PCCP

ROYAL SOCIETY OF CHEMISTRY

PAPER

View Article Online
View Journal | View Issue

Cite this: *Phys. Chem. Chem. Phys.*, 2020, **22**, 24480

Charge transport mechanisms in potassium superoxide

Zongxiang Hu, Wenchang Tan,* Shunning Li * and Feng Pan *

Received 2nd July 2020,
Accepted 29th September 2020

DOI: 10.1039/d0cp03540h

rsc.li/pccp

Rechargeable metal–air batteries based on superoxide discharge products are attractive due to the facile one-electron redox process of O_2/O_2^-. Recently, a K–O_2 battery has been reported that showed a significantly lower discharge/charge potential gap than the Li–O_2 battery systems. Here, we perform first-principles calculations on potassium superoxide (KO_2) to unravel the charge transport mechanism in this discharge product. The concentration and mobility of intrinsic carriers are calculated. The results show that hole polarons and negatively charged potassium ion vacancies are the main charge carriers. The conductivity associated with polaron hopping (2×10^{-12} S cm^{-1}) is 8 orders of magnitude higher than that of Li_2O_2, and the ionic conductivity has a comparable value (1×10^{-13} S cm^{-1}). Our calculation results can rationalize the experimental findings and provide a theoretical basis for the understanding of superoxide discharge products in metal–air batteries.

1 Introduction

Non-aqueous metal–air batteries are attracting more attention in recent years as a potential energy storage technology. Among all the metal-air systems, lithium-air (Li–O_2) batteries have been regarded as the most appealing one due to their higher energy density than the other ones. The theoretical specific energy density of Li–O_2 batteries is approximately 8 times that of traditional lithium-ion batteries (LIBs). However, the practical energy density of a Li–O_2 battery is limited by the low conductivity of the discharge product, lithium peroxide (Li_2O_2). Moreover, the discharge process includes reduction of oxygen to superoxide (LiO_2) and its further disproportionation into Li_2O_2 and O_2, while the charging process is characterized by direct oxidation of Li_2O_2 to O_2.[1–4] This asymmetric reaction mechanism results in different overpotentials between charge (~1–1.5 V) and discharge (~0.3 V) processes, which corresponds to a low reversible energy efficiency of about 60%.[5,6]

Li_2O_2 is the main discharge product of the cathode of Li–O_2 batteries.[7–13] As a wide bandgap insulator, the electrical conductivity of Li_2O_2 mainly depends on the hopping of hole polarons and negatively charged Li-ion vacancies.[14–18] *Via* density functional theory (DFT) calculations, Garcia Lastra *et al.* found that the hole polaron in Li_2O_2 has higher mobility than the electron polaron.[15] Radin and Siegel estimated the intrinsic conductivity of Li_2O_2 by using the hybrid functional to investigate the concentration and mobility of the main charge carriers.[14] They found that hole polaron and lithium ion vacancies are the main carriers; the low concentration and limited mobility of these species lead to the low conductivity of Li_2O_2. This theoretical result was confirmed by experiments.[19] The electronic conductivity contributed by hole polaron migration is only 5×10^{-20} S cm^{-1}, which is equivalent to the conductivity of quartz glass on the order of magnitude.[19] Another discharge product, LiO_2, is not thermodynamically stable, which was generally neglected in previous studies on lithium-air batteries.[2,20–25] However, recent studies have explored the potential use of LiO_2 as a main discharge product for lithium–air batteries by using graphene as a substrate and metallic iridium nanoparticles as a catalyst.[26] Theoretical studies have found that the oxygen dimer vacancy is the main carrier for ionic conduction, which has higher mobility and conductivity than the hole polaron.[27] Although lithium-ion vacancies can also provide a certain degree of ionic conductivity, their contribution is inferior as compared with oxygen dimer vacancies. Theoretical results revealed that the conductivity of charge carriers in LiO_2 is much higher than that of Li_2O_2, which rationalized the experimental observation of lower overpotentials for batteries with LiO_2 discharge product than those with Li_2O_2. Recent studies also reported that Li_2O could be a main discharge product of the cathodes such as silicene and two-dimensional Tl_2O, which showed excellent electrochemical performance in the oxygen reduction reaction (ORR) and oxygen evolution reaction (OER).[28,29] In sodium–air (Na–O_2) battery systems, the ionic conductivity of NaO_2 was found to be about 10 orders of magnitude higher than Na_2O_2.[30] Therefore, we can deduce that superoxides are more promising as discharge products than their peroxide counterparts. It would be

School of Advanced Materials, Peking University, Shenzhen Graduate School, Shenzhen 518055, People's Republic of China. E-mail: tanwch@pku.edu.cn, lisn@pku.edu.cn, panfeng@pkusz.edu.cn

tempting if we can utilize superoxides with high thermodynamic stability in metal–air batteries. Potassium superoxide, KO_2, which is not only much more stable than LiO_2 and NaO_2 according to the soft and hard acid–base (HSAB) theory, but also allows for one-electron redox process of O_2/O_2^- in a potassium–air battery, which can be expected to open up a new world of opportunity for non-aqueous metal–air batteries.

Compared with Li–O_2 batteries, research on KO_2 is rather scarce.[31,32] Experiments have shown that the cathode with KO_2 as the discharge product has a significantly lower over-potential than that of Li–O_2 batteries.[31] The former has a voltage difference of approximately 50 mV during charging and discharging, while it is approximately 1 V for the latter. Although there may be multiple factors that lead to differences in overpotentials, in the present study, we still focus on carrier migration which we believe plays the dominating role.

Previous studies have calculated and analyzed the band structure of Li_2O_2.[26,33,34] But these studies did not give consistent results because of the different calculation methods they used. For example, the electronic structure of Li_2O_2 calculated by the traditional DFT method exhibits metallic properties, while the calculation using the HSE hybrid functional predicts a wide bandgap.[33] Because the traditional DFT method tends to delocalize the electrons and ignores the interaction between electrons, which is inaccurate for some metal oxides, the HSE hybrid functional would be more reliable, as demonstrated in previous works.[35]

In this work, we employed first-principles calculations to analyze the formation and migration of electron and hole polarons in KO_2, calculate the concentration and mobility of ionic carriers, and obtain the theoretical conductivity of KO_2. We compare the calculation results of KO_2 with those of Li_2O_2 in the literature and analyze how the difference in conductivity between them affects the macroscopic performance of the electrodes. Through further analysis of the carrier mobility, we can understand the charge conduction mechanism of the electrodes, and provide a theoretical basis for explaining the differences in overpotentials between different electrodes. These results will provide some inspiration and guidance for the experimental research on metal–air batteries with superoxide discharge products in the future.

2. Methodology

2.1 Computational details

Our calculations were performed using the plane-wave based DFT method as implemented in the Vienna *ab initio* simulation package (VASP) with Projector Augmented Wave (PAW) potentials.[36,37] The Perdew–Burke–Ernzerhof (PBE) parametrization of the generalized gradient approximation (GGA) was used to describe the electron exchange and correlation.[38,39] An energy cutoff of 460 eV was used for expanding the plane-wave basis set, and the *K*-point sampling density with an $8 \times 8 \times 8$ mesh within the Monkhorst–Pack scheme was used.[40] During the structural relaxation steps, a convergence threshold of 0.02 eV $Å^{-1}$ was reached in all residual forces during our calculation.

Research studies on Li_2O_2, LiO_2, Na_2O_2, and NaO_2 have pointed out that the HSE hybrid functional was crucial for describing the electronic structures.[14,16,17,27,30,32] Therefore, it is necessary to use the HSE hybrid functional to study the conduction mechanism of KO_2. To adequately characterize the localization of the polarons, charge-state defects, and polaron hopping barriers, we use the Heyd–Scuseria–Ernzerhof (HSE) screened hybrid functional.[41] Many aspects of alkali-metal superoxides such as lattice constants, band gaps, and charge localization can be improved by mixing a fraction of screened nonlocal Hartree–Fock (HF) exchange with the semi-local exchange in the HSE functional.[14,27] As a common practice, many-body perturbation theory (GW) was employed to obtain a more accurate bandgap.[42] The spin-polarized calculations were applied in all calculations, and it was found that the ferromagnetic configuration is more stable than the antiferromagnetic order with an energy difference of 200 meV.

For all the calculations of point defects within the supercell, a single *k*-point at Γ in the irreducible Brillouin zone was used. All defect structures were optimized *via* the HSE functional to maintain consistency with the electronic structure calculations. In the process of simulating charged defects, the introduction of a net charge or electric dipole in the supercell will inhibit the system from providing accurate total energy, which makes the total energy in different systems incomparable. Therefore, we adopt the method of Leslie *et al.* in the simulation of charged defects.[43] In this method, if a net charge is introduced into the supercell, it is necessary to add a neutral background charge with the opposite sign to maintain the overall electrical neutrality. However, the electrostatic energy between the net charge and its mirror image converges more slowly with the size of the simulated cell, which means that only in very large supercells can the calculation results be close to the actual situation without periodic boundary conditions. To correct this error, we adopted the method proposed by Makov and Payne,[44] which is simply referred to as the MP correction term.

2.2 Defect concentration

To obtain the equilibrium defect concentration and evaluate the stability of different charge states, we need to calculate the defect formation energies of polarons and point defects with different charges. The formation energy of a defect X^q in the charge state q is expressed as follow:[45–47]

$$E_f[X^q] = E_{tot}[X^q] - E_{tot}[P] - \sum_i n_i\mu_i + q\left(E_{F_VBM} + \varepsilon_{VBM}\right) + E_{MP} \quad (1)$$

where $E_{tot}[X^q]$ and $E_{tot}[P]$ are the total energies of the supercell containing a defect X^q and the pristine supercell, respectively. n_i is the number of defect specie i and μ_i is its corresponding chemical potential. E_{F_VBM} is the Fermi level referenced to the valence band maximum (VBM) of the bulk, and is bound between the VBM and the conduction band minimum (CBM), *i.e.*, $0 < E_{F\_VBM} < E_g$, where E_g is the bandgap. The first-order Makov–Payne correction was included to compensate for the spurious energy of aperiodic systems.[44]

When handling the chemical potential of oxygen, it should be noted that DFT fails to calculate the exact energy of oxygen molecules. A previous research study has reported the formation energy per oxygen atom calculated in HSE (α = 0.48) at 0 K *versus* the formation enthalpy measured in the standard state, 298 K and 1 atm.[33,48] For oxides, peroxides and superoxides, the experimental and calculated formation enthalpies should be ideally identical. However, DFT calculation tends to overestimate the chemical potential of oxygen in the gas phase, which makes the calculated formation enthalpies deviate from corresponding experimental values. By fitting the enthalpy data of various oxides, a slope of 1.003 and *y*-intercept of 0.468 was obtained. Thus, we can obtain a corrected oxygen chemical potential by compensating E_{correct} = 0.468 eV per oxygen atom according to the relationship between the experimental and calculated enthalpy of formation.[33] Finally, the chemical potential of oxygen in the gas phase in the standard state was given by the following formula:[33,48]

$$\mu_{\text{O}}{}^{0}(298\ \text{K}, 1\ \text{atm}) = \frac{1}{2}\left(E_{\text{O}_2}^{\text{cal}} + 2E_{\text{correct}} - TS_{\text{O}_2}{}^{0}\right) \quad (2)$$

where $E_{\text{O}_2}^{\text{cal}}$ is the calculated energy of O_2 by the HSE functional, $S_{\text{O}_2}{}^{0}$ is the entropy of oxygen that can be obtained by the first-principles calculation,[28] but we adopt a value obtained from the experiments ($-TS_{\text{O}_2}{}^{0}$ = −0.63 eV under standard conditions, 298 K and 1 atm) so as to keep with the previous works on peroxides and superoxides.[14,27,30,33,48] The chemical potential of potassium in KO_2 is determined by the relationship $\mu_{\text{K}}(\text{KO}_2) = E_{\text{tot}}[\text{KO}_2] - 2\mu_{\text{O}}$,[27] where $E_{\text{tot}}[\text{KO}_2]$ is the total energy of bulk crystal KO_2 per unit formula.

In thermodynamic equilibrium, the concentration of a defect is given as a function of its formation energy:[45,47]

$$c = N_{\text{sites}}\text{e}^{-E_{\text{f}}/k_{\text{B}}T} \quad (3)$$

where N_{sites} is the number density of defects in the supercell, E_{f} corresponds to the formation energy of a given defect, k_{B} is Boltzmann's constant, and T is the temperature.

2.3 Defect mobility

The mobility of a given defect can be determined by activation barriers along the minimum energy pathway that is obtained using the nudge elastic band (NEB) method from HSE functional calculation. The mobility of a given defect is expressed by the following formula:[49]

$$\mu = \frac{\nu Ze(\Delta x)^2}{k_{\text{B}}T}\text{e}^{-E_{\text{b}}/k_{\text{B}}T} \quad (4)$$

where ν is the hopping frequency with a value of about 10^{13} Hz, which equals to the atomic vibration at room temperature. Δx is the hopping distance, Ze is the charge of the defect, and E_{b} is the diffusion barrier of the hopping. The conductivity due to charged defects moving through a crystal is then given by the following formula:[49]

$$\sigma = c\mu Ze \quad (5)$$

3. Results and discussion

3.1 Structure and the oxygen dimer

X-ray diffraction data indicates that KO_2 crystallizes in the CaC_2-type tetragonal structure with the *I*4/*mmm* (see Fig. 1a) space group at room temperature, in which one alkali-metal atom provides one electron to an oxygen molecule and the resulting O_2^- molecular ion plays the role of an anion.[50,51] However, with one electron in the highest-occupied degenerate orbital of an oxygen molecule, KO_2 will be unstable and will undergo a distortion to form a system of lower symmetry and lower energy. The previous study also showed that the O_2^- dimers will rotate and the K ions in the *z*-direction also distort in the direction opposite to the oxygen dimer due to electrostatic interactions, and finally, KO_2 is stabilized by strong Coulomb correlation between K ions and O_2^- dimers.[50] Here, to obtain a rational ground-state of KO_2, we rotated the O_2^- dimers along the *z*-direction to allow for symmetry breaking during the structural relaxation process, as shown in Fig. 1b. The optimized structure is 0.92 eV lower in energy than the high-symmetry structure in Fig. 1a. Consequently, we use the structure shown in Fig. 1b for all calculations. A 3 × 2 × 3 supercell consisting of 108 atoms (Fig. 1c) was constructed to simulate point defects.

Oxygen ions in ordinary metal oxides are usually independent O^{2-} ions, with an eight-electron close shell configuration. Therefore, it is generally difficult to change the valence of oxygen ions. The distance between oxygen and oxygen in KO_2

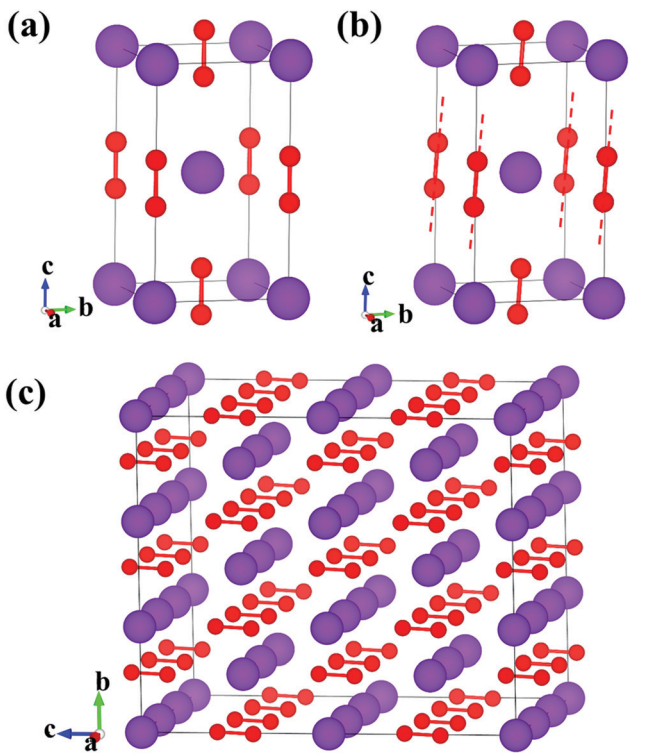

Fig. 1 Crystal structures of the (a) unit cell with a CaC_2 type (b) stable unit cell. (c) A 3 × 2 × 3 supercell. Red spheres represent oxygen atoms and purple spheres are potassium atoms.

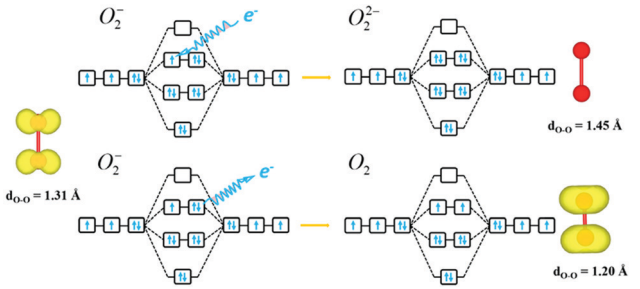

Fig. 2 Molecular orbital (MO) diagrams of oxygen (O_2^0), superoxide (O_2^-), and peroxide (O_2^{2-}) dimers.

is much smaller than the corresponding distance in ordinary metal oxides. Therefore, oxygen forms a dimer to form ionic molecules O_2^- through O–O bonding. The superoxide ion O_2^- is equivalent to an ordinary "oxygen molecule" carrying an electron. The orbital arrangement of the "oxygen molecule" is already familiar to us. The bonding orbital of the molecule is $(\sigma_g 2p_x^2)(\pi_u 2p_y^2)(\pi_u 2p_z^2)$ occupied by 6 electrons, and the remaining 2 electrons occupy the anti-bonding orbital $(\pi_g^* 2p_y^1)(\pi_g^* 2p_z^1)(\sigma_u 2p_x^0)$. Since there are two unpaired electrons in the two anti-bonding orbitals, O_2^0 has a total spin magnetic moment of 2 μB. In Fig. 2 we present the electron arrangement diagram and magnetic moment density diagram of oxygen molecules. The superoxide ion O_2^- is an ion molecule formed by an anti-bonding orbital π* occupied by one more electron. Comparing the electron arrangement of oxygen molecules, we can see that the electrons occupying the antibonding orbital of the superoxide ion π* are paired with the original electrons, and the spins are arranged in an antiparallel manner. Thus the superoxide ion has a 1 μB spin magnetic moment. From the magnetic moment density diagram in Fig. 2, we can also see that the magnetic moment density is reduced relative to the oxygen molecules. Occupation of electrons in the anti-bonding state leads to longer O–O bond lengths than oxygen molecules. The anti-bonding orbital of the O_2^- ion can still be occupied by another electron to form a peroxo ion. The peroxo ion O_2^{2-} does not exhibit magnetic moment density because all the electrons are paired. The O–O bond length is also elongated due to the occupied anti-bonding state. The π* orbitals of the oxygen dimer in KO_2 are partially occupied, which provides the possibility of a variable valence state for the oxygen dimer. If electrons and holes can be localized to the π* orbital of the oxygen dimer in the KO_2 bulk material, electrons and hole polarons will be formed. Similar to other alkali metal peroxides and peroxides, electron transport is controlled by the transformation among the three different charge states of the oxygen dimer: O_2^{2-}, O_2^- and O_2^0.

3.2 Electronic structure and bandgaps

First, the bulk properties of KO_2 are examined. The band structure obtained using the HSE functional is provided in Fig. 3. The HSE functional predicts an insulating feature of KO_2 with a large bandgap of 4.2 eV by splitting the π* states of oxygen. We tested four values for α: 0.25, 0.35, 0.48, and 0.60, whose influence on the bandgap is linear (Fig. 3b). Here, a fraction of 48% exact exchange (α = 0.48) for HSE calculations was adopted based on previous calculations in which Radin and Siegel first obtained an accurate bandgap of 3.6 eV for Li_2O_2. It should be noticed that the tetragonal phase of KO_2 (Fig. 1a) remains metallic even in HSE calculation. The GW method can give more accurate results for the band gap. Considering that the forbidden band of KO_2 cannot be predicted by PBE, we chose the G_0W_0@HSE06 method to perform a non-self-consistent GW calculation based on the HSE06 results.[52] Using this method, the forbidden bandwidth of KO_2 is calculated to be 5.0 eV.

3.3 Intrinsic defects in KO_2

The following intrinsic defects in KO_2 were considered in the calculations: electron polarons (e_P^-), hole polarons (h_P^+), O vacancies (V_O), O_2 vacancies (V_{O_2}), K vacancies (V_K), and

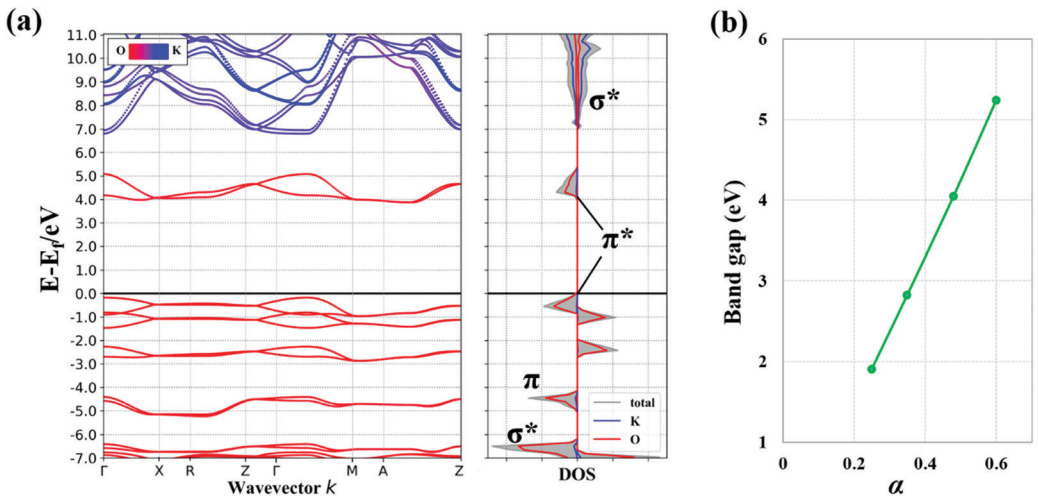

Fig. 3 (a) Electronic band structure and density of states plots of bulk KO_2 in HSE (α = 0.48) calculations. The Fermi level is located at zero energy. Red and blue lines represent the O and K bands, respectively. (b) The relationship between the band gap of KO_2 and the mixing parameter α.

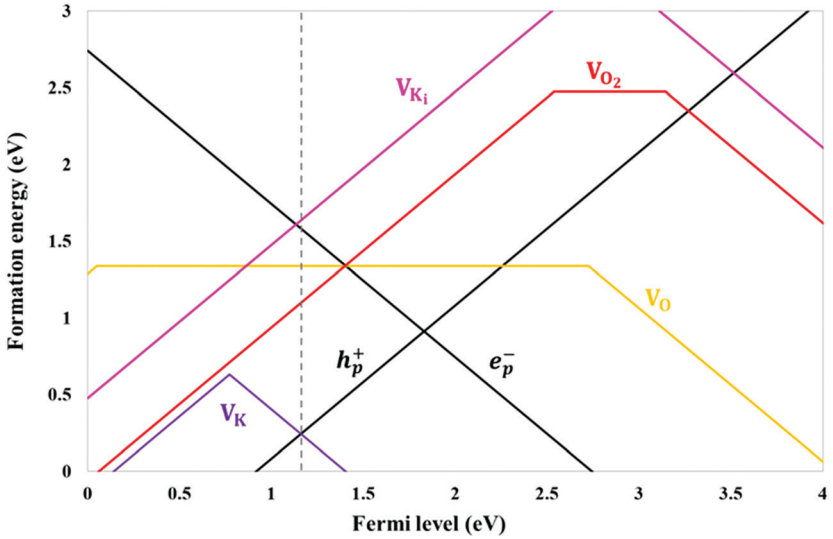

Fig. 4 Calculated formation energies of intrinsic defects in KO_2 as a function of the Fermi level. The vertical dashed line indicates the position of the Fermi level where charge neutrality is maintained.

K interstitials (K_i). Different charge states of these defects were taken into account. The calculated formation energies of various intrinsic point defects, in all possible charge states as a function of the Fermi level in KO_2, are shown in Fig. 4, from which we can derive the Fermi levels and the corresponding formation energies of various intrinsic defects under charge neutrality conditions. The horizontal lines represent the defects without charge, while the slope lines represent charged defects in which a positive (negative) slope indicates a defect with the positive (negative) charge. At a fixed Fermi level, only one charge state is thermodynamically stable for each defect. Therefore, only the segment corresponding to the lowest-energy charged state is shown. From Fig. 4, it can be found that hole polarons (h_P^+) and negative potassium vacancies (V_K^-) are more energetically favorable than other corresponding charged defects. In equilibrium, the concentrations of various defects should keep the KO_2 system electrically neutral, which is referred to as the charge neutrality condition.[47] Under this condition, the Fermi level is determined to be 1.16 eV by hole polarons (h_P^+) and negative potassium vacancies (V_K^-), as indicated by the vertical dashed line in Fig. 4.

3.4 Polarons

Polarons are self-trapped small charge carriers, which can be obtained by removing an electron from the O_2^- dimer (localized hole doping) or localizing an extra electron on the O_2^- dimer (localized electron doping), in a manner similar to previous studies for polarons in peroxides and superoxides.[26,27,34] With localized hole (electron) doping on the valence-band (conduction-band) of the O_2^- dimer, a new dimer O_2 (O_2^{2-}) forms, and the bond length of the dimer will be significantly changed. For the hole polaron, the O–O bond length decreases to 1.20 Å, while for the electron polaron, the O–O bond length increases to 1.45 Å. The magnetization density distribution can reflect the changes in the charge state of the oxygen dimers (Fig. 5), in which the isosurface of polarons shows the distinguished differences in the magnetic moment shapes of O_2^-, O_2 and O_2^{2-}.[53] When adding one electron on the partially occupied π^* orbital of O_2^- to form O_2^{2-}, all electrons are coupled and the original magnetism disappears, whereas on removing one electron from the π^* orbital of O_2^-, two single electrons in the two spin channel will correspond to a larger magnetic moment.

From the above results, we can see that the excess electrons and holes in KO_2 will be localized on the oxygen dimer to form small polarons, and will not affect the surrounding oxygen dimers. These small polarons in KO_2 are the same as those in Li_2O_2, LiO_2, Na_2O_2, and NaO_2. As shown in Fig. 5, the variable valence state of oxygen dimers are the key to the formation of

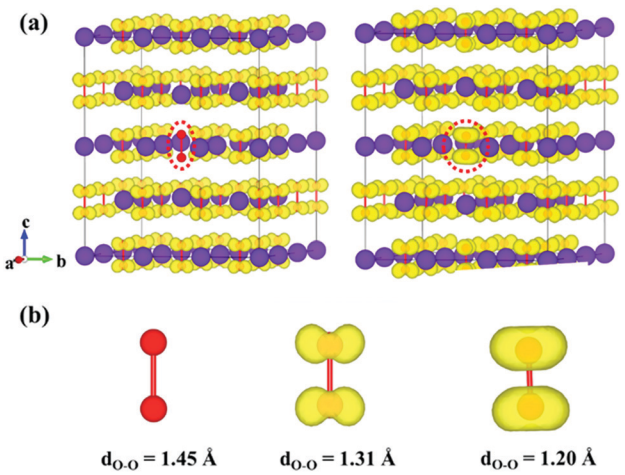

Fig. 5 Magnetization density distribution of (a) electron and hole polarons. (b) Structural and magnetic properties of O–O dimers with different charge states. The isosurfaces represent the spin density at the value of 0.03 e $Å^{-3}$. Red spheres represent oxygen atoms and purple spheres are potassium atoms.

small polarons. Moreover, the conductivity of KO_2 is closely related to the migration of polarons on the oxygen dimers, which will be discussed in detail later.

3.5 Vacancies and interstitials

In addition to electronic carriers, ion carriers also have an important impact on the electrical conductivity of KO_2. In addition to K ions, the ion carriers in KO_2 include all possible charged defects. In this section, we selected the following intrinsic defects for calculation: O vacancies (V_O), O_2 vacancies (V_{O_2}), K vacancies (V_K), and K interstitials (K_i). The different charge states of these defects were considered.

To understand the structural characteristics of various ionic defects and the relationship between them, an analysis of the magnetic moment density diagram (Fig. 6) is presented. V_K is formed by removing a neutral K atom in the supercell, which causes the nearest potassium ions and oxygen dimers to move into the vacant position, while the distant atoms show no significant displacement. Since removing neutral K atoms is equivalent to removing a K ion and doping a hole at the same time, we can find from the magnetic charge density that a nearby oxygen dimer has a non-uniform hole doping and an increase in the magnetic moment density. For V_K^-, the removal of a K ion leads to a similar structural change, but the magnetic moment density of all the oxygen dimers in the vicinity do not show significant change. When a V_K^+ defect is formed, it is equivalent to removing one K ion and doping two holes in the system. From the magnetic moment density two hole polarons are discernable.

O_2 vacancies show a different scenario from K vacancies. It can be seen that the magnetization density distributions of the nearest neighboring oxygen dimers rotate along the c axis, and simultaneously the neighboring K ions move toward the vacancy. By removing the O_2^- dimer, $V_{O_2}^+$ vacancies are formed and there is no polaron. When an O_2 dimer is removed from the supercell, the remaining electron forms an electron polaron in the other O_2^- dimer. $V_{O_2}^-$ vacancy is formed by the removal of $V_{O_2}^+$ from the supercell, so there are still two negative charges in other O_2^- dimers that form an electron polaron. Therefore, O_2 vacancies ($V_{O_2}^-$ vacancies) can be regarded as a complex of $V_{O_2}^+$ vacancies and electron polarons. O_2 vacancies are composed of $V_{O_2}^+$ vacancies and one electron polaron, and $V_{O_2}^-$ vacancies are composed of $V_{O_2}^+$ vacancies and two electron polarons. We calculated the binding energy of $V_{O_2}^+$ vacancies and electron polarons in V_{O_2} vacancies and $V_{O_2}^-$ vacancies according to $V_{O_2} \Leftrightarrow V_{O_2}^+ + h_P^-$ and $V_{O_2} \Leftrightarrow V_{O_2}^+ + 2h_P^-$. The calculated binding energies for V_{O_2} vacancies and $V_{O_2}^-$ vacancies are 0.21 eV and −0.10 eV, respectively. These results indicate that for the V_{O_2} vacancy it is difficult to release free-electron polarons while $V_{O_2}^-$ vacancy will dissociate into free $V_{O_2}^+$ vacancy and two electron polarons, showing the behavior of defect complexes.

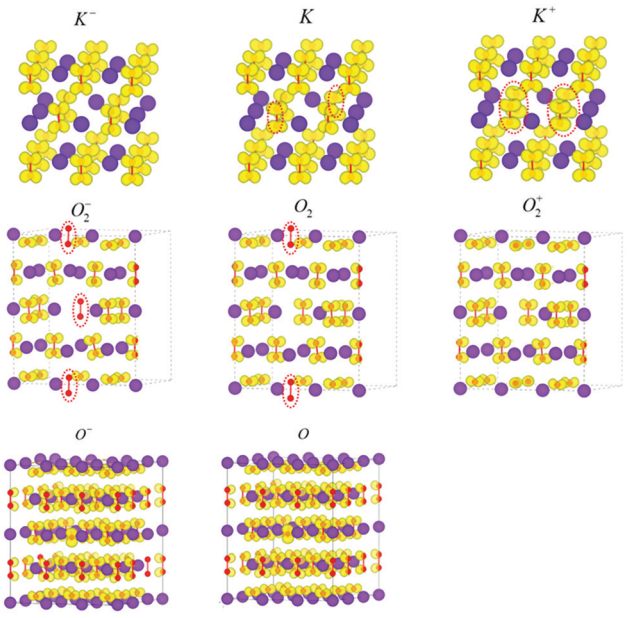

Fig. 6 Magnetization density distribution of K ion vacancies, K ion interstitials, oxygen vacancies, and oxygen dimer vacancies in KO_2. The isosurfaces are shown at a value of 0.03 e Å^{-3}. Red spheres represent oxygen atoms and purple spheres are potassium atoms.

A single O vacancy seems to exhibit a different behavior. The remaining oxygen ion in the V_O^- vacancy is reduced to a charge state of −2, which is also the stable state of the oxygen anions in most transition metals. In this case, because the oxygen atom acquires an eight-electron configuration, no magnetic moment is observed. For the neutral vacancy V_O^0, the oxygen atom has a charge state of −1 and has a magnetic moment of 1 μB, the density of which has the characteristic of the O-2p orbital. The shape of the magnetic moment density distribution diagram is similar to the hole polaron in the metal oxide.[54]

3.6 Migration of defects

Mobility in KO_2 can result from the migration of charged defects and/or hopping of small polarons. The diffusion barriers for small polarons (h_P^+ and e_P^-) and two dominant charged carriers (V_K^- and $V_{O_2}^+$) were calculated by the HSE functional. We first consider the migration of polarons. The migration of polarons occurs in a hopping manner between the adjacent oxygen dimers, which is equivalent to electron injection from one O_2^- dimer to its neighboring dimer. The O–O bond length changes simultaneously with the switching of magnetic moments on both dimers during polaron hopping. Here, four polaron hopping along different pathways and the corresponding diffusion barriers are demonstrated in Fig. 7. Path 1 along the b axis is the shortest hopping path with a distance of 3.8 Å, while Path 2 along the c axis is the longest with a distance of 6.8 Å. The calculated diffusion barrier of Path 4 for the electron polaron is the lowest with a value of 0.45 eV, while that along Path 2 is the highest with 0.64 eV. As compared with electron polarons, the diffusion barriers of hole polarons are relatively higher, for which the lowest value is 0.62 eV while the highest is 0.85 eV. The above results indicate that the behavior of the diffusion of polarons is anisotropic in KO_2. From Fig. 7, Path 4 as the second shortest diffusion path for both electron and hole polarons is energetically favorable.

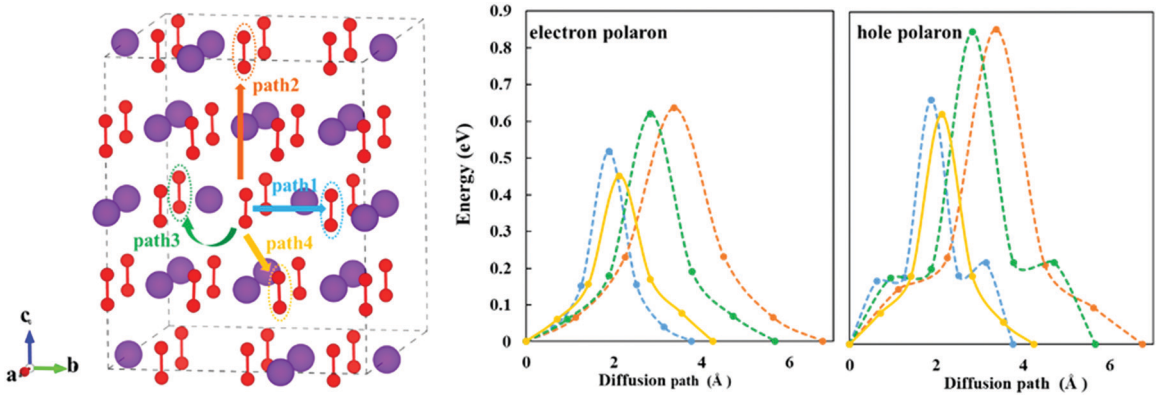

Fig. 7 Schematic representation and the calculated activation barriers for electron and hole polaron hopping along different directions. Red spheres represent oxygen atoms and purple spheres are potassium atoms.

Our results on polaron diffusion barriers are comparable to the reported diffusion barriers of 0.54–0.66 and 0.42–0.71 eV for electron and hole polarons in Li_2O_2, respectively.[14,18] Although the lowest barrier of polaron is slightly larger than that of Li_2O_2, the much greater concentration of hole polarons will significantly contribute to the electronic conductivity compared to Li_2O_2.

Vacancy defect migrations take place by exchanging the vacancy with its nearest neighbors between specie with the same vacancy. Fig. 8 shows the diffusion paths of two dominant charged vacancy carriers (V_K^- and $V_{O_2}^+$). For the diffusion of negative potassium vacancies, three anisotropic diffusion paths can be found in KO_2. Among these, the diffusion along the [1 1 1] direction (Path 3) shows the lowest barrier of about 0.69 eV. The second-lowest diffusion path is along the *b* axis (Path 2) with a barrier of about 0.72 eV. The slight discrepancy between their barriers implies that both paths are available for migration of V_K^-. Path 3 corresponds to three-dimensional diffusion that contributes to a preferred *b*-axis migration of V_K^-. Anisotropic diffusion is observed in the diffusion of positive dimer vacancy (Fig. 8b). A barrier as low as 0.25 eV along the [1 1 1] direction can demonstrate the facile diffusion of the oxygen dimers in KO_2, similar to the oxygen dimers in other superoxides.[27]

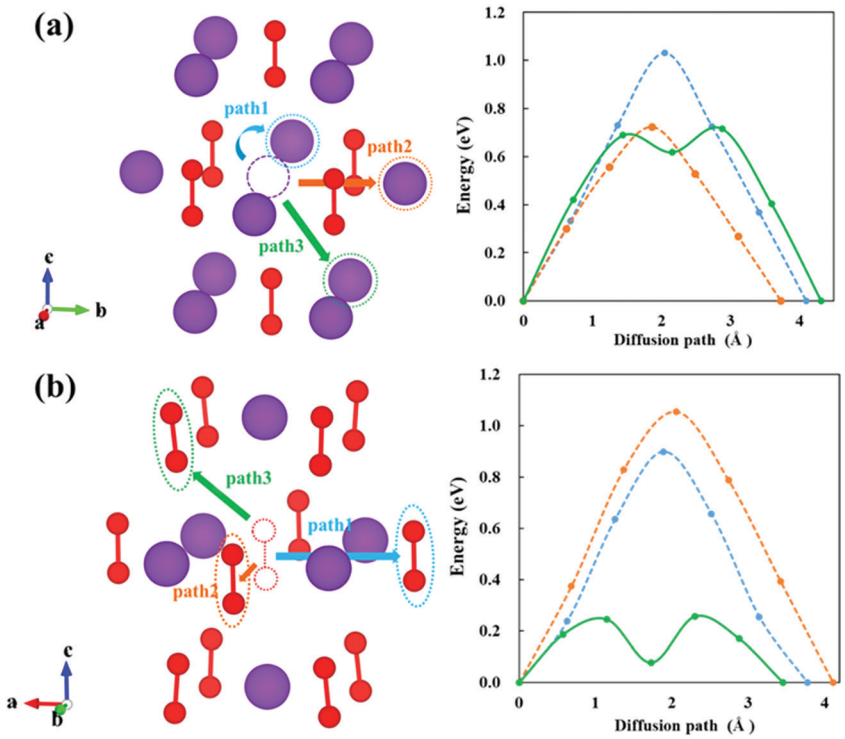

Fig. 8 Pathways for the diffusion of (a) V_K^- and (b) $V_{O_2}^+$ in KO_2 and the corresponding activation barriers. Red spheres represent oxygen atoms and purple spheres are potassium atoms.

3.7 Electronic and ionic conductivities

According to the formation energy of charge carriers, we calculated their concentrations using eqn (3), as tabulated in Table 1. The equilibrium concentrations of dominating charged carriers, h_P^+ and V_K^-, are estimated to be 1.66×10^{18} cm^{-3}, which is approximately 11 orders of magnitude greater than that of Li_2O_2.[14] The defects having the next-lowest formation energies are positive potassium vacancies (V_K^+) and O_2 vacancies ($V_{O_2}^+$). We found that the concentration of potassium interstitials is rather low because of their high formation energy of over 1.5 eV.

Under charge neutrality conditions, we can calculate the conductivity of KO_2 through the carrier concentration mobility calculated above. Our calculated mobility and conductivity are given in Table 2. The results show that the electronic conductivity of KO_2 is mainly contributed by the hole polaron, which is the same as in the cases of Li_2O_2,[14] Na_2O_2[30] and MgO_2.[55] The conductivity of the hole polaron in KO_2 is 2×10^{-12} S cm^{-1}, which is 8 orders of magnitude higher than the electronic conductivity of Li_2O_2.[14] Under actual circumstances, the working environment of the electrode will affect the position of the Fermi level, resulting in the deviation of the carrier concentration from the theoretical value. KO_2 has higher electron carrier mobility than Li_2O_2, and therefore it exhibits better electrical conductivity and better electrochemical performance than Li_2O_2.

The conductivities of ionic defects are given in Table 2 based on the carrier concentration and migration energy barrier. Although the migration of ionic defects is relatively facile, their conductivity is not high due to low defect concentration under equilibrium conditions. The calculated conductivity is 1×10^{-13} S cm^{-1}, and the K ion vacancy is the most important ionic charge carrier in KO_2. It is worth mentioning that the ionic conductivity of Li_2O_2 is 4×10^{-19} S cm^{-1}.[14] Therefore, both the electronic and ionic conductivities of KO_2 are much larger than the corresponding values of Li_2O_2 Table 3 summarizes the previously calculated electronic and ionic conductivities of Li_2O_2, LiO_2, Na_2O_2 and NaO_2. The calculated conductivity of KO_2 is consistent with previous experimental results (approximately 10^{-10} S cm^{-1}).[30]

Table 1 Formation energies (E_f, eV) and concentrations (c, cm^{-3}) (T = 300 K) of the relevant defects in KO_2 under the charge neutrality conditions

Defect	E_f (eV)	c (cm^{-3})	Defect	E_f (eV)	c (cm^{-3})
e_P^-	1.58	6×10^{-5}	h_P^+	0.24	2×10^{18}
V_K^-	0.24	2×10^{18}	V_O^-	2.90	4×10^{-27}
V_K	1.05	5×10^{4}	V_O	1.34	7×10^{-1}
V_K^+	1.02	2×10^{5}	$V_{O_2}^-$	4.46	3×10^{-53}
K_i^-	4.95	2×10^{-61}	$V_{O_2}^0$	2.47	6×10^{-20}
K_i^0	3.41	1×10^{-35}	$V_{O_2}^+$	1.10	7×10^{3}
K_i^+	1.64	7×10^{-6}			

Table 2 Calculated mobility (μ, cm^2 V^{-1} s^{-1}) and conductivity (σ, S cm^{-1}) of the relevant charge carriers in KO_2 at room temperature

Charge carrier	μ (cm^2 V^{-1} s^{-1})	σ (S cm^{-1})
e_P^-	4×10^{-9}	4×10^{-32}
h_P^+	6×10^{-12}	2×10^{-12}
V_K^-	5×10^{-13}	1×10^{-13}
$V_{O_2}^+$	1×10^{-5}	1×10^{-20}

Table 3 Calculated ionic and electronic conductivities (S cm^{-1}) of KO_2 and their comparison with prior calculations for Li_2O_2,[16] LiO_2,[27] Na_2O_2 and NaO_2[30]

Charge carrier	Ionic conductivity (S cm^{-1})	Electronic conductivity (S cm^{-1})
Li_2O_2	9×10^{-19}	5×10^{-20}
LiO_2	4×10^{-12}	3×10^{-12}
Na_2O_2	5×10^{-20}	1×10^{-20}
NaO_2	4×10^{-9}/1×10^{-10}	1×10^{-19}
KO_2	1×10^{-13}	2×10^{-12}

Our results indicate that the electrical conductivity of KO_2 is much higher than that of Li_2O_2. Since the electronic band structures indicate that they are insulating, when their grain size exceeds the critical value of the electron tunneling effect (5–10 nm),[56] electron conduction depends on polaron migration. On the one hand, the increase in conductivity can accelerate the chemical reaction of the electrode during charge and discharge to improve the rate performance. On the other hand, the overpotential can be regarded as a driving force that drives carrier migration. As the carrier mobility increases, the overpotential required by the electrode will inevitably become lower. Therefore, the high electrical conductivity of KO_2 may explain why the overpotential of the potassium air battery with KO_2 as the discharge product is lower than that of the lithium–air battery with Li_2O_2 as the discharge product.

For the ionic conductivity in KO_2, we found that the oxygen dimer vacancy is the ionic charge carrier with the highest mobility, but its relatively low concentration results in a lower contribution to conductivity. The K ion vacancy is the main ionic charge carrier in KO_2, and its mobility and conductivity are comparable to hole polarons. Therefore, K ions are easier to move in the KO_2 bulk phase than oxygen dimers. During the charging process, KO_2 will be oxidized. In the early stages, K ions will be extracted from KO_2 to form $K_{1-x}O_2$. The deintercalation mechanism of K ions is similar to that of traditional embedded electrode materials, and then the oxygen dimer will be released from the positive electrode. This is similar to the decomposition process of Li_2O_2, but the latter will undergo the intermediate phase of LiO_2, resulting in an asymmetric reaction during cycling.[34,57]

The hole polaron is the main electron carrier in KO_2, and has the highest mobility in the *b*-axis direction. The K ion also prefers diffusion along the *b*-axis. Accordingly, crystal growth along the *b* direction would be preferable for KO_2, which may lead to a larger capacitance and lower overpotential, as well as the reduction in the internal resistance of the battery. It should be noted that the relationship between the overpotential and carrier mobility is only an explanation for an experimental phenomena. Many possible factors may affect the overpotential, including the surface reaction rate and electrolyte decomposition.[8,58–61] Therefore, when optimizing the design of a potassium–air battery, many factors need to be considered,

and the mobility of charge carriers is only one of them. Nevertheless, we believe that our theoretical investigation on KO_2 will not only shed light on the design of K–O_2 batteries, but, when combined with previous studies, can also provide a common theoretical basis for the understanding of superoxide discharge products for different metal–air batteries.

4. Conclusion

Using the HSE hybrid functional, we have analyzed the electronic structure of KO_2, the formation energy and concentration of carriers, and the mobility of the main charge carriers. The partially-filled π^* orbitals of the structural unit, oxygen dimer O_2^-, provides the possibility of a variable valence state for O_2^-. Electrons and holes can be localized on the dimer in the KO_2 bulk material, thus forming small polarons. Some of the intrinsic defects are actually defect complexes formed by the combination of basic defects and small polarons. Under the condition of charge neutrality, the position of the Fermi level (1.16 eV) is determined, based on which we have calculated the equilibrium concentration of polarons and defects. The concentrations of hole polaron on the oxygen dimer and K ion vacancies are the highest (1.66×10^{18} cm^{-3}), followed by oxygen dimer vacancy. The migration of electronic and ionic charge carriers in KO_2 are anisotropic, and they prefer to migrate along the *b*-axis. Among these, the migration barriers of electron polaron and hole polaron are 0.45 and 0.62 eV, respectively. The migration barrier of $V_{O_2}^+$ is only 0.25 eV, which indicates that the oxygen dimer has exceedingly high mobility, but it does not contribute much to the overall conductivity due to its low concentration in KO_2. The hole polaron contributes to the electronic conductivity of KO_2, which is estimated to be 2×10^{-12} S cm^{-1}, and is 8 orders of magnitude higher than the electronic conductivity of Li_2O_2. The ionic conductivity of KO_2 is contributed by V_K^- and its value is 1×10^{-13} S cm^{-1}. The high electronic and ionic conductivity of KO_2 can rationalize the superior electrochemical performance of cathodes in K–O_2 batteries as compared with the Li–O_2 batteries.

Conflicts of interest

There are no conflicts to declare.

Acknowledgements

This work was financially supported by the National Key R&D Program of China (2016YFB0700600), and the Shenzhen Science and Technology Research Grant (ZDSYS201707281026184).

References

1 N. B. Aetukuri, B. D. McCloskey, J. M. García, L. E. Krupp, V. Viswanathan and A. C. Luntz, *Nat. Chem.*, 2015, **7**, 50–56.
2 L. Johnson, C. Li, Z. Liu, Y. Chen, S. A. Freunberger, P. C. Ashok, B. B. Praveen, K. Dholakia, J.-M. Tarascon and P. G. Bruce, *Nat. Chem.*, 2014, **6**, 1091–1099.
3 R. Black, S. H. Oh, J.-H. Lee, T. Yim, B. Adams and L. F. Nazar, *J. Am. Chem. Soc.*, 2012, **134**, 2902–2905.
4 C. O. Laoire, S. Mukerjee, K. M. Abraham, E. J. Plichta and M. A. Hendrickson, *J. Phys. Chem. C*, 2009, **113**, 20127–20134.
5 J. W. Fergus, *J. Power Sources*, 2010, **195**, 939–954.
6 H. Pan, Y.-S. Hu and L. Chen, *Energy Environ. Sci.*, 2013, **6**, 2338–2360.
7 P. G. Bruce, S. A. Freunberger, L. J. Hardwick and J. M. Tarascon, *Nat. Mater.*, 2012, **11**, 19–29.
8 A. C. Luntz and B. D. McCloskey, *Chem. Rev.*, 2014, **114**, 11721–11750.
9 Y. Y. Shao, S. Park, J. Xiao, J. G. Zhang, Y. Wang and J. Liu, *ACS Catal.*, 2012, **2**, 844–857.
10 K. M. Abraham and Z. Jiang, *J. Electrochem. Soc.*, 1996, **143**, 1–5.
11 N. Imanishi, A. C. Luntz and P. G. Bruce, *The lithium air battery*, Springer, New York, 2014.
12 G. Girishkumar, B. McCloskey, A. C. Luntz, S. Swanson and W. Wilcke, *J. Phys. Chem. Lett.*, 2010, **1**, 2193–2203.
13 J. Christensen, P. Albertus, R. S. Sanchez-Carrera, T. Lohmann, B. Kozinsky, R. Liedtke, J. Ahmed and A. Kojic, *J. Electrochem. Soc.*, 2012, **159**, R1–R30.
14 M. D. Radin and D. J. Siegel, *Energy Environ. Sci.*, 2013, **6**, 2370–2379.
15 J. M. Garcia-Lastra, J. S. G. Myrdal, R. Christensen, K. S. Thygesen and T. Vegge, *J. Phys. Chem. C*, 2013, **117**, 5568–5577.
16 J. B. Varley, V. Viswanathan, J. K. Nørskov and A. C. Luntz, *Energy Environ. Sci.*, 2014, **7**, 720–727.
17 S. P. Ong, Y. Mo and G. Ceder, *Phys. Rev. B: Condens. Matter Mater. Phys.*, 2012, **85**, 081105.
18 J. Kang, Y. S. Jung, S.-H. Wei and A. C. Dillon, *Phys. Rev. B: Condens. Matter Mater. Phys.*, 2012, **85**, 035210.
19 O. Gerbig, R. Merkle and J. Maier, *Adv. Mater.*, 2013, **25**, 3129–3133.
20 Z. Peng, S. A. Freunberger, L. J. Hardwick, Y. Chen, V. Giordani, F. Bardé, P. Novák, D. Graham, J.-M. Tarascon and P. G. Bruce, *Angew. Chem., Int. Ed.*, 2011, **123**, 6475–6479.
21 J. Yang, D. Zhai, H.-H. Wang, K. C. Lau, J. A. Schlueter, P. Du, D. J. Myers, Y.-K. Sun, L. A. Curtiss and K. Amine, *Phys. Chem. Chem. Phys.*, 2013, **15**, 3764–3771.
22 C. Xia, M. Waletzko, L. Chen, K. Peppler, P. J. Klar and J. Janek, *ACS Appl. Mater. Interfaces*, 2014, **6**, 12083–12092.
23 D. Zhai, H. H. Wang, K. C. Lau, J. Gao, P. C. Redfern, F. Kang, B. Li, E. Indacochea, U. Das, H. H. Sun, H. J. Sun, K. Amine and L. A. Curtiss, *J. Phys. Chem. Lett.*, 2014, **5**, 2705–2710.
24 T. Vegge, J. M. Garcia-Lastra and D. J. Siegel, *Curr. Opin. Electrochem.*, 2017, **6**, 100–107.
25 R. Gao, X. Liang, P. Yin, J. Wang, Y. L. Lee, Z. Hu and X. Liu, *Nano Energy*, 2017, **41**, 535–542.
26 J. Lu, Y. J. Lee, X. Luo, K. C. Lau, M. Asadi, H. H. Wang, S. Brombosz, J. Wen, D. Zhai, Z. Chen, D. J. Miller, Y. S. Jeong, J. B. Park, Z. Z. Fang, B. Kumar, A. Salehi-Khojin, Y. K. Sun, L. A. Curtiss and K. Amine, *Nature*, 2016, **529**, 377–382.

27 S. Li, J. Liu and B. Liu, *Chem. Mater.*, 2017, **29**, 2202–2210.
28 Y.-X. Yu, *J. Phys. Chem. C*, 2019, **123**, 205–213.
29 J.-H. Li, J. Wu and Y.-X. Yu, *J. Phys. Chem. C*, 2020, **124**, 9089–9098.
30 S. Yang and D. J. Siegel, *Chem. Mater.*, 2015, **27**, 3852–3860.
31 X. Ren and Y. Wu, *J. Am. Chem. Soc.*, 2013, **135**, 2923–2926.
32 O. Gerbig, R. Merkle and J. Maier, *Adv. Funct. Mater.*, 2015, **25**, 2552–2563.
33 B. Lee, J. Kim, G. Yoon, H.-D. Lim, I.-S. Choi and K. Kang, *Chem. Mater.*, 2015, **27**, 8406–8413.
34 W. Fan, B. Wang, X. Guo, X. Kong and J. Liu, *Nano Energy*, 2016, **27**, 577–586.
35 A. I. Liechtenstein, V. I. Anisimov and J. Zaanen, *Phys. Rev. B: Condens. Matter Mater. Phys.*, 1995, **52**, R5467–R5470.
36 P. E. Blöchl, *Phys. Rev. B: Condens. Matter Mater. Phys.*, 1994, **50**, 17953–17979.
37 G. Kresse, M. Marsman and J. Furthmüller, *VASP the GUIDE*, Universitat Wien, Vienna, 2016.
38 G. Kresse and J. Furthmüller, *Comput. Mater. Sci.*, 1996, **6**, 15–50.
39 J. P. Perdew, K. Burke and M. Ernzerhof, *Phys. Rev. Lett.*, 1996, **77**, 3865–3868.
40 H. J. Monkhorst and J. D. Pack, *Phys. Rev. B: Condens. Matter Mater. Phys.*, 1976, **13**, 5188–5192.
41 J. Heyd, G. E. Scuseria and M. Ernzerhof, *J. Chem. Phys.*, 2003, **118**, 8207–8215.
42 M. Shishkin and G. Kresse, *Phys. Rev. B: Condens. Matter Mater. Phys.*, 2006, **74**, 035101.
43 M. Leslie and N. J. Gillan, *J. Phys. C: Solid State Phys.*, 1985, **18**, 973–982.
44 G. Makov and M. C. Payne, *Phys. Rev. B: Condens. Matter Mater. Phys.*, 1995, **51**, 4014–4022.
45 C. G. Van de Walle and J. Neugebauer, *J. Appl. Phys.*, 2004, **95**, 3851–3879.
46 S. Lany and A. Zunger, *Phys. Rev. B: Condens. Matter Mater. Phys.*, 2008, **78**, 235104.
47 C. Freysoldt, B. Grabowski, T. Hickel, J. Neugebauer, G. Kresse, A. Janotti and C. G. Van de Walle, *Rev. Mod. Phys.*, 2014, **86**, 253–305.
48 S. Kang, Y. Mo, S. P. Ong and G. Ceder, *Nano Lett.*, 2014, **14**, 1016–1020.
49 R. J. D. Tilley, *Defects in Solids*, John Wiley & Sons, New Jersey, 2008.
50 M. Kim and B. I. Min, *Phys. Rev. B: Condens. Matter Mater. Phys.*, 2014, **89**, 121106(R).
51 J. S. Kang, D. H. Kim, J. H. Hwang, J. Baik, H. J. Shin, M. Kim, Y. H. Jeong and B. I. Min, *Phys. Rev. B: Condens. Matter Mater. Phys.*, 2010, **82**, 193102.
52 F. Fuchs, J. Furthmueller, F. Bechstedt, M. Shishkin and G. Kresse, *Phys. Rev. B: Condens. Matter Mater. Phys.*, 2007, **76**, 115109.
53 D. Larcher and J. M. Tarascon, *Nat. Chem.*, 2015, **7**, 19–29.
54 J. B. Varley, A. Janotti, C. Franchini and C. G. Van de Walle, *Phys. Rev. B: Condens. Matter Mater. Phys.*, 2012, **85**, 081109.
55 J. G. Smith, J. Naruse, H. Hiramatsu and D. J. Siegel, *Chem. Mater.*, 2017, **29**, 3152–3163.
56 V. Viswanathan, K. S. Thygesen, J. S. Hummelshoj, J. K. Norskov, G. Girishkumar, B. D. McCloskey and A. C. Luntz, *J. Chem. Phys.*, 2011, **135**, 214704.
57 M. Olivares-Marin, A. Sorrentino, R. C. Lee, E. Pereiro, N. L. Wu and D. Tonti, *Nano Lett.*, 2015, **15**, 6932–6938.
58 B. D. McCloskey, J. M. Garcia and A. C. Luntz, *J. Phys. Chem. Lett.*, 2014, **5**, 1230–1235.
59 J. S. Hummelshoj, J. Blomqvist, S. Datta, T. Vegge, J. Rossmeisl, K. S. Thygesen, A. C. Luntz, K. W. Jacobsen and J. K. Norskov, *J. Chem. Phys.*, 2010, **132**, 071101.
60 S. A. Freunberger, Y. Chen, Z. Peng, J. M. Griffin, L. J. Hardwick, F. Bardé, P. Novák and P. G. Bruce, *J. Am. Chem. Soc.*, 2011, **133**, 8040–8047.
61 Y.-C. Lu and Y. Shao-Horn, *J. Phys. Chem. Lett.*, 2013, **4**, 93–99.